Journal of Solid State Chemistry **163,** 300–307 (2002)
doi:10.1006/jssc.2001.9414, available online at http://www.idealibrary.com on IDEAL®

$Bi_{0.85}Ln_{0.15(1-n)}V_{0.15\,n}O_{1.5+0.15n}$ Fluorite Type Oxide Conductors: Stability, Conductivity, and Powder Crystal Structure Investigations

M. Benkaddour, S. Obbade,[1] P. Conflant, and M. Drache

Laboratoire de Cristallochimie et Physicochimie du Solide, UPRES A 8012, ENSCL et USTL, B.P. 108, 59652 Villeneuve d'Ascq Cedex, France

Received July 2, 2001; in revised form September 26, 2001; accepted September 28, 2001

To extend the study of Bi_2O_3–Ln_2O_3–V_2O_5 systems, an investigation of $Bi_{0.85}Ln_{0.15(1-n)}V_{0.15n}O_{1.5+0.15n}$ materials (Ln = La, Pr, Nd, Sm, Tb, Ho, Yb), which adopt a fluorite-related structure for specific composition ranges, has been realized. The composition dependence of thermal stability of the structure evidenced using thermodiffractometry, and of conductivity properties determined from impedance spectroscopy, has been investigated. The pure anionic oxide conductor behavior evidenced by emf measurements of an oxygen concentration cell for $Bi_{0.85}Pr_{0.105}V_{0.045}O_{1.545}$ mixed oxide can be considered for other samples containing other rare earths. X-ray powder crystal structure refinements have been realized for praseodymium-containing terms $Bi_{0.85}Pr_{0.15(1-n)}V_{0.15n}O_{1.5+0.15n}$; $n = 0.1, 0.3, 0.5$) and for a selection of the other lanthanide elements (Ln = La, Sm, Tb, Ho, and Yb) with $n = 0.3$, on the basis of the Willis model. The stability and modification of the crystal structure are discussed. © 2002 Elsevier Science

INTRODUCTION

Among the four crystalline varieties (α, β, γ, δ) announced for the bismuth sesquioxide, the δ-Bi_2O_3 form stable between 729 and the melting point 827°C is well known for its attractive anionic conduction properties (1), attributed to the oxygen-deficient and highly disordered fluorite type structure (2). Partial cationic substitutions for Bi^{3+} have been investigated for numerous systems (3–15) aiming to preserve in the room temperature range the high-temperature structure and therefore the significant conduction properties. According to Watanabe the disordered δ-structure cannot really be stabilized at room temperature and each preserved fcc phase corresponds to a metastable variety (16, 17). The results obtained for Bi–Ln–V–O (14) or Bi–Sm–M–V–O (M = Ni, Co, Pb) (15) mixed oxides are in good agreement with the existence of two fluorite-related structures.

The well-known δ-type phase modification for the binary systems when the bismuth content increases (structure stability enhancement and conductivity decrease) led us to consider that a 85 mol% Bi_2O_3 ratio is optimal for the preparation of promising materials (14)

The investigation of the conductivity–composition correlation for the series $Bi_{0.85}Ln_{0.105}V_{0.045}O_{1.545}$ (Ln = Sm to Yb) reveals a small increase of isothermal σ with the Ln size but also higher conductivity performances for Ln = Tb ($\sigma = 10^{-3}$ S·cm^{-1} at 300°C) likely due to the specific electronic structure of this element which allows two oxidation states. On the basis of this work, higher interesting conductivity properties could be expected for mixed oxides with the largest ionic radii (Ln = La, Pr, Nd), especially for Pr, which like Tb presents mixed oxidation states. This led us to extend the previous investigation (14) to the $Bi_{0.85}Ln_{0.15(1-n)}V_{0.15n}O_{1.5+0.15n}$ mixed oxides with $n = 0.1$, 0.3, and 0.5 for Pr and $n = 0.3$ for the other lanthanide elements. For electrical properties investigation, we took into account the results of a recent study in which an influence of powder granulometry on the densification and a resistance–compactness dependence of ceramics have been observed (18).

Structural refinements were done on the basis of $(Bi_2O_3)_{0.75}(Gd_2O_3)_{0.25}$ (19) and $(Bi_2O_3)_{0.80}(Ho_2O_3)_{0.20}$ (20) mixed oxides investigations, in agreement with the Willis model (21,22). A discussion has been realized aiming to correlate the structural characteristics with thermal stability and conductivity properties of the materials.

EXPERIMENTAL

Using the preheated Bi_2O_3, V_2O_5, and lanthanide oxides, polycrystalline samples (≅3 g) of fcc $Bi_{0.85}Ln_{0.15(1-n)}V_{0.15n}O_{1.5+015n}$ phases ($n = 0.1$, 0.3, 0.5 for Ln = Pr and $n = 0.3$ for Ln = La, Nd, Sm, Tb, Ho, or Yb) were prepared by three successive 15-hours treatments at 700, 800, and 840–950°C (depending on the considered sample). Samples were finally air-quenched. The purity of the fcc phase was verified by powder X-ray diffraction using a Guinier de Wolff camera (Cu$K\alpha$ radiation).

[1] To whom correspondence should be addressed. Fax: (33) 320436814. E-mail: obbade@ensc-lille.fr.

0022-4596/02 $35.00

Powder X-ray diffraction data of each sample were recorded at room temperature on a Siemens D5000 diffractometer using a Bragg-Brentano geometry with diffracted beam monochromatized Cu$K\alpha$ radiation. The diffraction patterns were collected by steps of 0.02°(2θ) over the angle range 20°–130°, with a counting time of 40 s per step. In order to minimize the preferential orientation effects which can occur when powdered samples are pressed, the samples were finely ground and then sieved to 30–40 μm to get a homogeneous grain size, and a bottom loading method was used.

The thermal behavior of samples was examined on the basis of combined investigations of X-ray thermodiffraction patterns, and $\log \sigma = f(1000/T)$ Arrhenius plots, with examination of materials X-ray diffraction patterns after every conductivity measurement.

X-ray thermodiffraction studies were carried out using a Siemens D5000 X-ray diffractometer equipped with a HTK10 high-temperature device and a Guinier-Lenné camera. In the first case (HTK10), the isothermal recordings were undertaken in the range 20–800°C with 100°C steps, in air gas flow with a platinum sample holder; resulting from the duration of the isothermal data collecting and of the samples heating from 20 to 800°C, the average heating rate was nearly 400°C/h for all samples. Using a Guinier-Lenné camera, the thermal behavior investigation has to be realized with a slow heating rate. The measurements conditions were thus: continuous recording in 20–900°C temperature range in static air; gold grid sample holder; heating rate, 15°C/h. From data recorded using the diffractometer, the cell parameter has been accurately refined on the basis of a fcc cell for each isothermal recording.

Electrical measurements were realized on cylindrical pellets of ceramic materials made using a conventional press and then sintered at 900°C for 15 hours, and finally air-quenched.

Oxygen transport numbers were determined from emf values of an "air/electrolyte material/oxygen" cell with material pellet characteristics: diameter 11–12 mm, thickness ca. 3 mm, and compactness ca. 90%. Air and oxygen electrode gases were exchanged after 5–minutes flow sweeping. Two series of measurements were carried out: the first one was realized versus temperature using air and oxygen; the second series was done after a long treatment at 500°C (2 weeks), with air and oxygen diluted in nitrogen.

The pellets used for investigation of the conductivity properties of $Bi_{0.85}Ln_{0.105}V_{0.045}O_{1.545}$ materials (Ln = La, Sm, Gd, Tb, Ho, Yb) were elaborated from powder with grain sizes optimized using the attrition procedure previously described (18). In each case, a significant amount of sample was prepared (≅25 g) to limit the pollution from the grinding media (balls of tetragonal yttria–zirconia polycrystals, diameter 2 mm). The powder attrition treatment was realized for 3 hours (attrition speed 1000 rpm), using an ethanolic slurry of material (24 wt. %). Each sample was dried for 60 hours in an oven (70–80°C). After pellet elaboration, sintering, and air-quenching, the compactness ranged between 95 and 96% for all samples. Both flat surfaces of pellets (diameter 5 mm, thickness ca. 3 mm) were equipped with gold electrodes deposited using a sputtering method. The conductivity was determined by impedance spectroscopy in the range 1–10^6 Hz using a Solartron SI 1255 Schlumberger response analyzer; each set of values was recorded at a given temperature after 1 hour of stabilization (300–800°C, 20°C step).

The crystal structure refinements were carried out with the Rietveld profile refinement technique (23, 24) by means of the program FULLPROF (25) based on version DbW3.2S (8804) of the Rietveld code published by D. B. Wiles and R. A. Young (26, 27). The peak shape was represented by a pseudo-Voigt function with an asymmetry correction at low angles. In order to describe the angular dependence of the peak full-width at half- maximum (H), the formulation of Caglioti *et al.* (28) was used: $H^2 = U\tan^2\theta + V\tan\theta + W$ where U, V, and W parameters were refined in the process. The background was adjusted by refinement of the polynomial function coefficients of 5° in 2θ. The procedure involved the refinement of other parameters (scale factor, effective 2-theta zero of the instrument, atomic coordinates, cell parameters, and thermal parameters). At the end of each refinement, the good matching between observed and calculated data was indicated by the significant values of the profile reliability factors (R_p, R_{wp}) and the crystal structure model quality factors (R_F, R_{Bragg}).

RESULTS AND DISCUSSION

A pure $Bi_{0.85}Ln_{0.15(1-n)}V_{0.15n}O_{1.5+0.15n}$ fluorite type phase has been obtained by sample air-quenching for all investigated $Bi_{0.85}Ln_{0.105}V_{0.045}O_{1.545}$ materials (Ln = La, Pr, Nd, Sm, Tb, Yb). The composition range of pure fluorite type phase has been determined for Ln = Pr ($0.1 \le n \le 0.7$) and Ln = Nd ($0 \le n \le 0.5$); for Ln = La, the compositional domain of the fluorite phase, likely narrow in the range ($0.3 + \varepsilon \le n \le 0.3 - \varepsilon$), has not been determined. Taking into account the composition dependence of the stability and of the conductivity performances evidenced for the $Bi_{0.85}Ln_{0.105}V_{0.045}O_{1.545}$ homologous families (Ln = Y, Sm–Dy, Er, Yb) (14), the study of the Pr-based materials was limited to the domain $0.1 \le n \le 0.5$ for which three samples (n = 0.1, 0.3, and 0.5) were examined.

From X-ray data recorded for all synthesized samples, the cell parameter has been refined. It is observed that the substitution of Pr^{3+} and Nd^{3+} by V^{5+} (smaller cation) leads to a diminishing of the a cell parameter obeying Vegard's law, although an increase of the oxide number occurs. A linear diminution of density is also observed

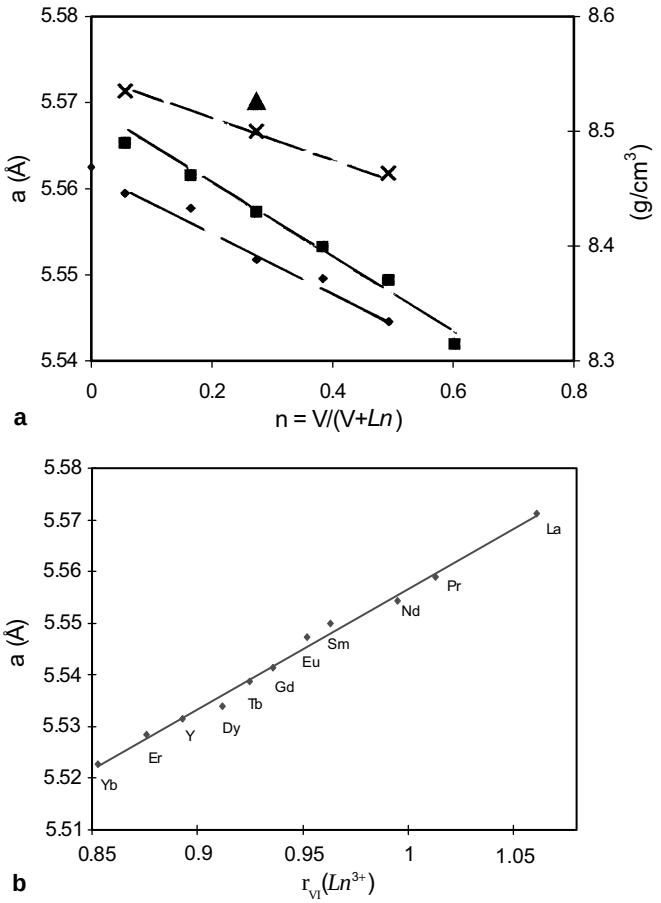

FIG. 1. (a) $Bi_{0.85}Ln_{0.15(1-n)}V_{0.15n}O_{1.5+0.15n}$ cell parameter (Ln = La (▲), Pr (■), Nd (◆)) and density (Ln = Pr, n = 0.1, 0.3, 0.5). (b) Evolution versus Ln^{3+} radius of cell parameter for $Bi_{0.85}Ln_{0.105}V_{0.045}O_{1.545}$ (Ln = La, Pr, Nd, Sm, Eu, Gd, Tb, Dy, Er, Yb, and Y).

(Fig. 1a). Such a behavior has been observed by N. Portefaix *et al.* (14) for homologous families with Ln = Sm, Eu, and Gd. Moreover, the linear dependence of the cell parameter versus the Ln^{3+} cationic radius (Ln = Y, Sm, Eu, Gd, Tb, Dy, Er, Yb) for the series $Bi_{0.85}Ln_{0.105}V_{0.045}O_{1.545}$, evidenced by these authors, implies also a linear correlation between a and the mean cationic radius, and appears confirmed when large lanthanides (La, Pr, and Nd) are also considered (Fig. 1b).

The thermal behavior investigation, using X-ray thermodiffractometry, has evidenced the influence of the composition and of the heating–cooling rate of the treatment with respect to the fcc structure stability.

A thermal study between 20 and 800°C realized for 2 hours (average heating rate 400°C/h), using the Siemens diffractometer equipped with its HTK10 high-temperature device, allows us to maintain the fcc single phase for all samples, in the whole investigated temperature range. The temperature dependence of the lattice constant, presented for six selected samples in Fig. 2, evidences two linear domains analogously to those already observed for $Bi_{0.85}Eu_{0.1}V_{0.05}O_{1.55}$ and $Bi_{0.85}Gd_{0.105}V_{0.045}O_{1.545}$ (14). This dependence has been attributed to the existence of an order–disorder rearrangement which affects only the light atoms of the structure (i.e., the oxide ions). With increasing n the rearrangement temperature increases (Fig. 2a). No significant Ln dependence of the break point temperature has been observed (Fig. 2b). The thermal expansion coefficients, which appear to be independent of the Ln nature, are nearly 1.2×10^{-5} and $1.9 \times 10^{-5}\,°C^{-1}$ for the low- and high-temperature ranges, respectively.

Investigation of $Bi_{0.85}Pr_{0.15(1-n)}V_{0.15n}O_{1.545+0.15n}$ samples during slow heating treatments (15°C/h) has been realized using a Guinier-Lenné camera (Fig. 3). A partial transformation of the fcc fluorite structure into a rhombohedral Bi–Sr–O type phase has been observed at almost

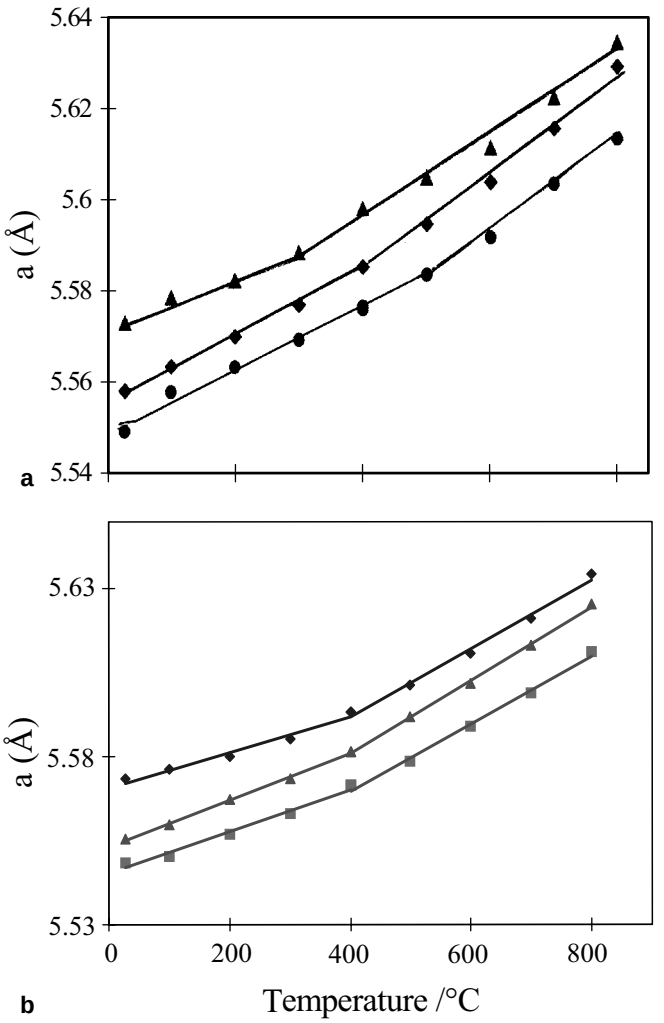

FIG. 2. Cell parameter evolution versus temperature (a) for $Bi_{0.85}Pr_{0.15(1-n)}V_{0.15n}O_{1.5+0.15n}$ (n = 0.1, ▲; 0.3, ◆; 0.5, ●) and (b) for $Bi_{0.85}Ln_{0.105}V_{0.045}O_{1.545}$ (Ln = La (◆), Sm (▲), and Gd (■)).

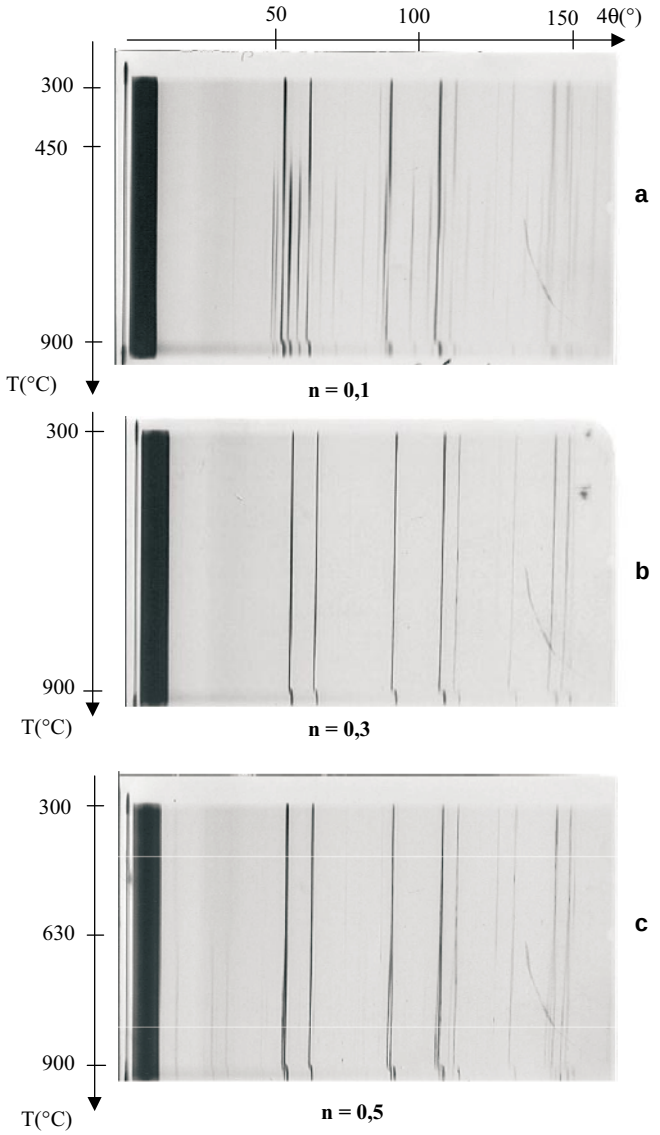

FIG. 3. Guinier–Lenné X-ray pattern of $Bi_{0.85}Pr_{0.15(1-n)}V_{0.15n}O_{1.5+0.15n}$ ($n = 0.1$, 0.3, 0.5).

450°C with $n = 0.1$ (Fig. 3a). For sample $Bi_{0.85}Pr_{0.105}V_{0.045}O_{1.545}$ ($n = 0.3$), no transformation occurred in the whole investigated temperature range 20–900°C (Fig. 3b). A crystal structure transformation has been evidenced for material with $n = 0.5$ nearly 630°C (Fig. 3c). The new phase, which is observed up to 900°C, may be preserved at room temperature whatever the cooling treatment; a hexagonal crystalline cell has been identified ($a = 6.7475(2)$ Å, $c = 9.7397(3)$ Å) for this phase; the powder X-ray diffraction pattern data are reported in the Table 1.

The evolution of the emf of an oxygen concentration cell with $Bi_{0.85}Pr_{0.105}V_{0.045}O_{1.545}$ as electrolyte has been investigated versus the temperature for a given gradient of oxygen pressure, and versus the gradient of oxygen pressure during an isothermal treatment at 500°C.

Figure 4a, which reports the evolution of $t_{O^{2-}}$ ionic transport number versus the temperature, corresponds to the case of a study with air and oxygen as gaseous electrodes. The average heating–cooling rate was nearly 25°C/h. Only the $t_{O^{2-}}$ values calculated for the temperature range 500–800°C correspond to stabilized emf; these values are almost 1 during the heating run, whereas a decrease happens below 575°C during cooling. The departure between the values determined during the heating run and those of the cooling treatment can result from various facts such as a material annealing which leads to pellet surfaces porosity modification, or a partial phase transformation when an oxygen pressure higher than 0.2 atm is applied, or both phenomena together. So a Guinier de Wolff X-ray diffraction pattern realized after the measurements cycle has evidenced, besides the fluorite type phase, some traces of a sillenite type phase; this second phase, which is well known to be an electronic conductor, could be responsible for the significant diminishing of the emf during cooling.

Figure 4b allows us to compare the experimental and the calculated evolution of the measured voltage versus $\log(P_{O_2})$, (P_{O_2} = oxygen partial pressure of the first electrode compartment when the second one contains air). Taking into account the experimental conditions used for the measurements, a good gas-tight cell appears improbable;

TABLE 1
Observed and Calculated X-Ray Powder Diffraction Pattern for Hexagonal Compound $Bi_{0.85}Pr_{0.075}V_{0.075}O_{1.575}$

h	k	l	d_{obs} (Å)	d_{cal} (Å)	I_{obs}/I_0 (%)
0	0	3	3.2463	3.2460	39
1	0	1	3.1892	3.1891	100
1	0	2	2.7740	2.7740	61
1	0	4	1.9742	1.9745	23
1	1	0	1.9493	1.9487	25
1	0	5	1.6870	1.6869	11
1	1	3	1.6709	1.6708	26
2	0	1	1.6635	1.6629	13
0	0	6	1.6228	1.6230	3
2	0	2	1.5947	1.5946	10
2	0		1.4963	1.4974	1
2	0	4	1.3870	1.3870	6
1	0	7	1.2864	1.2862	3
2	0	5	1.2754	1.2754	5
2	1	1	1.2648	1.2649	7
1	1	6	1.2472	1.2471	6
2	1	2	1.2339	1.2341	5
2	1	4	1.1298	1.1300	4
2	1	5	1.0674	1.0672	3
3	0	3	1.0632	1.0630	3
3	0	5	0.9742	0.9742	2
1	1	9	0.9459	0.9460	3
2	1	7	0.9403	0.9402	3

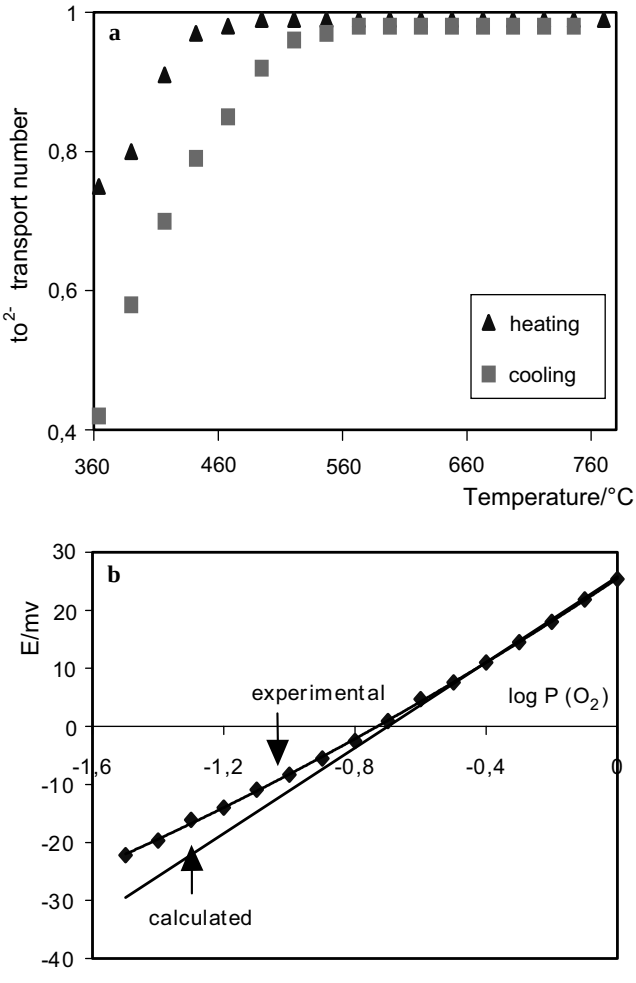

FIG. 4. (a) $t_{O_{2-}}$ ion transport number evolution of $Bi_{0.85}Pr_{0.105}V_{0.045}O_{1.545}$ versus temperature during a heating (▲) and a cooling (■) process. (b) Emf–P_{O_2} dependence for an oxygen concentration cell with $Bi_{0.85}Pr_{0.105}V_{0.045}O_{1.545}$ as electrolyte.

this could be responsible for the small departure between the two considered evolutions.

Unambiguously, the Bi–Pr–V–O sample ($n = 0.3$) appears to be a pure oxide conductor when it is used as a solid electrolyte of an oxygen concentration cell. A similar behavior is highly likely for the other Bi–*Ln*–V–O materials examined in this paper when no phase transformation occurs.

Transport number and conductivity conditions of the measurement are similar to those of X-ray thermodiffraction study (Guinier-Lenné). From Arrhenius plots of the conductivity we observe two different behaviors: For each material $Bi_{0.85}Ln_{0.105}V_{0.045}O_{1.545}$ (*Ln* = La, Pr, Sm, Gd, and Tb) the good similarity of three successive Arrhenius plots characterizes the stability of the δ-structure (Fig. 5a). For homologous materials with *Ln* = Ho and Yb (Fig. 5a) and for Pr-containing samples with $n = 0.1$ and 0.5 (Fig. 5b), the electrical behavior characterizes the δ-phase transformation during a slow cooling, proved by the X-ray diffraction of residues after each conductivity measurement.

The decrease of the conductivity during the heating run, which characterizes the partial transformation "fluorite type-$\delta \rightarrow$ Bi–Sr–O type phase" for $n = 0.1$ (Figs. 3a and 5b), disappears for $n = 0.3$. For higher vanadium content ($n = 0.5$), once again a decrease of σ is observed; it corresponds to the formation of the new hexagonal phase identified during the X-ray thermodiffractometry study. It is difficult to determine an evident conductivity level–composition correlation. For the first heating run, below the temperature of δ-phase transformation, a small decrease of σ occurs when n increases. In the high-temperature range, samples $n = 0.1$ and 0.3 present a similar conductivity ($\sigma \cong 0.25$ S.cm^{-1}); the weak conductivity level observed for sample $n = 0.5$ (Fig. 5b) results from the formation of the hexagonal new phase during the thermal treatment of this material.

An evident correlation between the *Ln* size and the oxide conductivity level of the fluorite type phase is observed for the $Bi_{0.85}Ln_{0.105}V_{0.045}O_{1.545}$ materials, essentially in the high-temperature domain. In the low-temperature range, the low σ level observed for the Ho and Yb samples results from the presence of a second minor phase that we did not identify, besides the fluorite type phase. Moreover, the influence of the pellet compactness, evidenced in the recent study of $Bi_{0.85}Pr_{0.105}V_{0.045}O_{1.545}$ material, is confirmed by the slight difference of the σ level observed for $Bi_{0.85}Ln_{0.105}V_{0.045}O_{1.545}$ materials, respectively, with compactness nearly 95–96% in this study, and nearly 80% (14).

Powder X-ray diffraction profile refinements have been carried out at room temperature using the fluorite-related structural Willis model. According to this model, 4*a* sites (0, 0, 0) are statistically occupied by four cations, and oxygen atoms over 32*f* sites of the *Fm*3*m* group (x, x, x; $x = \frac{1}{4} + \delta$) with an occupancy number in agreement with the formulas. For the mixed cationic site occupied by Bi, *Ln* (*Ln* = La, Pr, Sm, Tb, Ho, or Yb), and V atoms the occupancy numbers were fixed to fit the nominal composition of each sample. The evaluation of the oxide anions number was done on the basis of one oxidation state only for each metallic element (Bi^{3+}, Ln^{3+}, and V^{5+}), presuming that all prepared samples exhibit a pure ionic conductor behavior, like the $Bi_{0.85}Pr_{0.105}V_{0.045}O_{1.545}$ material. At the end of the refinement process, the agreement between observed and calculated data was characterized by the reliability factors R_{Bragg}, R_F. These data are displayed in Table 2 with the refined cell parameters for all investigated samples. Table 3 groups their characteristic atomic coordinates, occupancy numbers, and isotropic thermal parameters. Resulting from the oxide location in 32*f* sites, the nearest cationic environments are characterized by short and long (Bi, *Ln*, V)–O distances; these couples are reported in Table 4 with the

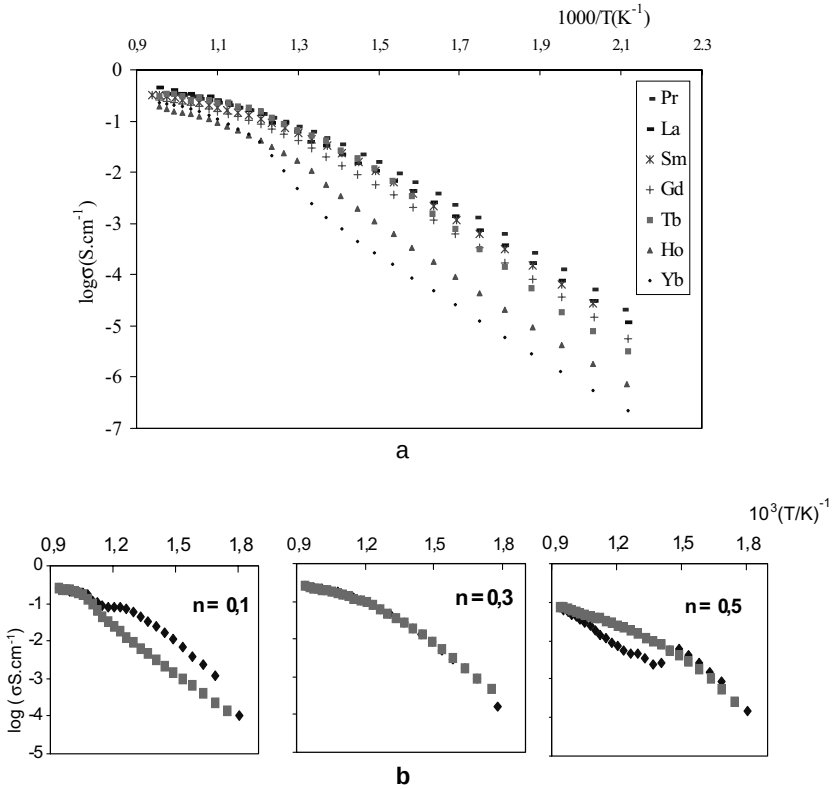

FIG. 5. Arrhenius plots (a) for cooling run for $Bi_{0.85}Ln_{0.105}V_{0.045}O_{1.545}$ (Ln = La, Pr, Sm, Tb, Yb) and (b) for a heating (◆) and cooling (■) cycle for $Bi_{0.85}Pr_{0.15(1-n)}V_{0.15n}O_{1.5+0.15n}$ (n = 0.1, 0.3, 0.5).

mean radii $(Bi, Ln, V)_{VI}$ (in hexacoordination) calculated from the Shannon data (29, 30).

For the Pr compound, the weak cell parameter diminution (0.3% for $n = 0.1$ to 0.5) shows that the cationic size effect is quite counterbalanced by the oxide number increase.

A qualitative discussion can be done on results obtained using X-ray as well as neutron diffraction data. Neutron diffraction studies of δ-Bi_2O_3 (2, 31) and Bi_2O_3–Er_2O_3-related compounds (32, 33), realized from a starting fluorite type model "oxygen sites ($\frac{1}{4}, \frac{1}{4}, \frac{1}{4}$) 25% randomly vacant," revealed supplementary interstitial oxygen sites $32f$ (x, x, x; $x = \frac{1}{4} + \delta$) for Bi_2O_3, and $32f$ and $48i$ ($\frac{1}{2}, x, x$) for Bi_2O_3–Ln_2O_3 compounds; moreover, for these lanthanide-based phases, a displacement of the cations, first introduced in $4a$ (0, 0, 0) sites, to $24e$ (x, 0, 0) positions was also evidenced.

TABLE 2
Lattice Constants and Reliability Factors for $Bi_{0.85}Ln_{0.15(1-n)}V_{0.15n}O_{1.5+0.15n}$ Rietveld Structure Refinements (S.G.: *Fm3m*)

Ln	*n*	*a* (Å)	R_{Bragg}	R_F
	0.1	5.5644(1)	0.052	0.055
Pr	0.3	5.5501(1)	0.063	0.065
	0.5	5.5495(1)	0.063	0.065
La		5.5662(1)	0.075	0.067
Sm		5.5453(2)	0.065	0.059
Tb	0.3	5.5324(1)	0.050	0.052
Ho		5.5264(1)	0.063	0.052
Yb		5.5156(1)	0.072	0.065

TABLE 3
Characteristic Atomic Coordinates, Occupancy Factors, and Isotropic Thermal Parameters for $Bi_{0.85}Ln_{0.15(1-n)}V_{0.15n}O_{1.5+0.15n}$ Materials

		Occupancy number				*x*, *x*, *x* (O)	B_{iso} (Å²)	
Ln	*n*	*Bi*	*Ln*	V	O	*x*	(Bi, *Ln*, V) Site	O Site
	0.1	3.40	0.54	0.06	6.06	0.314(2)	3.21(3)	1.81(1)
Pr	0.3	3.40	0.42	0.18	6.18	0.300(2)	3.65(3)	2.87(6)
	0.5	3.40	0.30	0.30	6.30	0.297(2)	3.22(3)	1.83(2)
La						0.330(2)	2.89(4)	1.0(6)
Sm						0.300(5)	2.63(4)	5(1)
Tb	0.3	3.40	0.42	0.18	6.18	0.304(4)	2.53(4)	5(1)
Ho						0.321(2)	2.38(3)	4(1)
Yb						0.322(2)	3.50(4)	3(1)

TABLE 4
Characteristic (Bi, *Ln*, V)–O Distances for $Bi_{0.85}Ln_{0.15(1-n)}V_{0.15n}O_{1.5+0.15n}$ Materials

Ln	*n*	(Bi, *Ln*, V) r_{VI} mean (Å)	(Bi, *Ln*, V)–O (Å)	(Bi, *Ln*, V)–O (Å)
	0.1	1.012	2.279(7)	3.027(7)
Pr	0.3	0.998	2.288(9)	2.887(9)
	0.5	0.983	2.292(8)	2.857(8)
La		1.003	2.273(9)	3.180(9)
Sm		0.993	2.29(3)	2.89(3)
Tb	0.3	0.988	2.28(2)	2.91(2)
Ho		0.985	2.26(1)	3.07(1)
Yb		0.982	2.25(1)	3.07(1)

The $(Bi_2O_3)_{0.80}(Er_2O_3)_{0.20}$ thermal investigation in the range 27–827°C led Verkerk *et al.* (32) to the conclusion that there is no long-range ordering of vacancies; short-range ordering appears at low temperatures, with the occurrence of relatively short *Ln*–O distances, whereas the oxygen lattice disorders above 597°C. This polymorphism was characterized by two evolution domains of the cell parameter versus temperature. The phase transition between the two forms was linked to a bend in the log $\sigma = f(1000/T)$ Arrhenius plot. Another investigation relative to structural refinements of this material quenched or aged (2 weeks at 500°C annealing treatment) (33) shows that the distributions of oxide ions over the three anionic sites allow us to distinguish quenched and annealed structures. The 48*i* sites are similarly occupied for both sample types ($\cong$12% of anions) but the distributions of the remaining oxygen atoms over sites 8*c*/32*f* are different. Both sites are occupied (33/54% of anions) for quenched sample, analogously to $(Bi_2O_3)_{0.73}(Y_2O_3)_{0.27}$ treated for 1 day at 500°C (31), whereas only 32*f* sites are significantly occupied (87% of anions) for annealed samples.

Using our $Bi_{0.85}Pr_{0.15(1-n)}V_{0.15n}O_{1.5+015n}$ X-ray data, no supplementary oxygen site (8*c* or 48*i*) could be observed. The temperature dependence of the cell parameter, with two almost linear domains for each investigated sample (Fig. 2), similarly to that observed for $(Bi_2O_3)_{0.80}$–$(Er_2O_3)_{0.20}$ (32) or for samples $Bi_{0.85}Ln_{0.105}V_{0.045}O_{1.545}$ (14) or $Bi_{0.85}Sm_{0.105}V_{0.018}Pb_{0.027}O_{1.5045}$ (15), is in good agreement with this hypothesis; the breaking point between the two domains, observed at about 400°C for the used heating conditions, has to be attributed to an order $\rightarrow$ disorder transition. In contrast, this transition is not clearly evidenced from the log $(\sigma) = f(1000/T)$ Arrhenius plots (Figs. 5a and 5b) which correspond to measurements during thermal treatments realized using weaker rates ($\cong 20°h^{-1}$). This indicates that the kinetics of the ordering or disordering transformation are slow and therefore can occur over a wide temperature range during dynamic thermal treatments.

The δ-phase structure stability appears to be linked to the length of the *long* (Bi, *Ln*, V)–O distances; the shorter these are, the more stable the structure. So, the V^{5+} for Ln^{3+} substitution which shortens these distances increases the stability, whereas long bonds such as for Ho- or Yb-containing samples appear to decrease the stability. For $Bi_{0.85}Pr_{0.105}V_{0.045}O_{1.545}$, the *long* (Bi, Pr, V)–O distance (2.887 Å) is significantly shorter than the corresponding one determined for the $Bi_{0.8}Ho_{0.2}O_{1.5}$ fluorite type sample (3.46 Å), which has the interesting δ-phase structure stability.

It has been shown for other series of materials that a decrease of the ratio ionic volume/cell volume can be linked to a conductivity performance improvement (34, 35). For the $Bi_{0.85}Ln_{0.105}V_{0.045}O_{1.545}$ series, the monotonic decrease of this ratio from Yb- to La-based samples corresponds to an increase of σ from Yb- to Sm-based samples; for Pr- and La-based materials no change is observed. This phenomenon could be related to the diminishing of the cationic polarizability, which is an important parameter for the conductivity of the bismuth-based fluorite type oxide phases.

CONCLUSION

This investigation on the $Bi_{0.85}Ln_{0.15(1-n)}V_{0.15n}O_{1.5+015n}$ materials has revealed significant information.

These materials obtained at room temperature by air-quenching adopt a fluorite type structure in composition ranges depending on the *Ln* nature: $0.1 \leq n \leq 0.7$ for Pr, $0.1 \leq n \leq 0.5$ for Nd, $0.3 - \varepsilon \leq n \leq 0.3 + \varepsilon$ for La. The detailed study of three Pr-based terms ($n = 0.1$, 0.3, and 0.5) has shown that the preserved structure is metastable; its "stability" depends on the composition and on the rate of the thermal treatment. Fast thermal treatment from 20 to 800°C for 2 hours allows us to keep the structure in the three cases studied and to discern two temperature–cell parameter evolution domains; they can be attributed to both low-temperature ordered and high-temperature disordered forms with a transition near 400°C. For low rates (15–20°C/h), an X-ray thermodiffraction investigation between 20°C and 800°C (stability domain of the structure) does not reveal any apparent crystal structure transformation for $n = 0.3$ when it occurs for other samples. This structure "stability" has also been characterized from the $\log(\sigma) = f(1000/T)$ Arrhenius plots examination for these samples as well as for the series of the $Bi_{0.85}Ln_{0.105}V_{0.045}O_{1.545}$ (*Ln* = La, Sm, Tb, Ho, Yb). The pure anionic oxide conductivity evidenced for $n = 0.3$ is also presumed for all samples.

The X-ray powder crystal structure refinements have been realized for these materials and discussed taking into account the previous published studies. Investigated samples seem to correspond to ordered phases. Two kinds of

(Bi, Pr, V)–O bonds (2.279–2.292 Å and 3.027–2.857 Å) are observed. The increase of the crystal structure "stability" during the V for Pr replacement has likely to be attributed to the significant contraction of the long bonds.

The evolution of the conductivity when $Bi_{0.85}Ln_{0.105}V_{0.045}O_{1.545}$ is examined can be linked to the evolution of the structure compactness and to the cationic polarization.

REFERENCES

1. T. Takahashi, H. Iwahara, and Y. Nagai, *J. Appl. Electrochem.* **2,** 97 (1972).
2. H. A. Harwig, *Z. Anorg. Allg. Chem.* **444,** 151 (1978).
3. T. Takahashi, H. Iwahara, and T. Arao, *J. Appl. Electrochem.* **5,** 187 (1975).
4. T. Takahashi, T. Esaka, and H. Iwahara, *J. Appl. Electrochem.* **5,** 197 (1975).
5. H. Iwahara, T. Esaka, T. Sato, and T. Takahashi, *J. Appl. Electrochem.* **39,** 173 (1981).
6. M. J. Verkerk and A. J. Burgraaf, *Solid State Ionics* **3/4,** 463 (1981).
7. A. Watanabe and T. Kikuchi, *Solid State Ionics* **21,** 287 (1986).
8. P. Conflant, C. Follet-Houttemane, and M. Drache, *J. Mater. Chem.* **1**(4), 649 (1991).
9. T. Takahashi and H. Iwahara, *J. Appl. Electrochem.* **3,** 65 (1973).
10. A. El Harrak, P. Conflant, M. Drache, and J. C. Boivin, *J. Chim. Phys.* **88,** 2281 (1991).
11. M. Omari, M. Drache, P. Conflant, and J. C. Boivin, *Solid State Ionics* **40/41,** 929 (1990).
12. G. Meng, C. Chen, X. Han, P. Yang, and D. Peng, *Solid State Ionics* **28/30,** 533 (1988).
13. D. Mercurio, M. El Farissi, B. Frit, J. M. Réau, and J. Senegas, *Solid State Ionics* **39,** 297 (1990).
14. N. Portefaix, P. Conflant, J. C. Boivin, J. P. Wignacourt, and M. Drache, *J. Solid State Chem.* **134,** 219 (1997).
15. M. Benkaddour, M. Omari, J. C. Boivin, P. Conflant, and M. Drache, *Ann. Chim. Sc. Mater.* **25**(1), 165–168 (2000).
16. A. Watanabe, *Solid State Ionics* **34,** 35 (1989).
17. A. Watanabe, *Solid State Ionics* **40–41,** 889 (1990).
18. M. Benkaddour, M. C. Steil, M. Drache, and P. Conflant, *J. Solid State Chem.* **155,** 273–279 (2000).
19. Y. Ito, T. Mukoyama, H. Mori, and K. Koto, *Solid State Ionics* **79,** 81 (1995).
20. K. Sooryanarayana, R. Somashekar, and T. N. Guru Row, *Solid State Ionics* **104,** 319 (1997).
21. B. T. M. Willis, *Proc. R. Soc.* **a274,** 134 (1963).
22. B. T. M. Willis, *Acta Crystallogr.* **18,** 75, (1965).
23. H. M. Rietveld, *Acta Crystallogr.* **22,** 151 (1967).
24. H. M. Rietveld, *J. Appl. Crystallogr.* **2,** 65 (1969).
25. J. Rodriguez-Carvajal, M. T. Fernandez-Diaz, and J. L. Martinez, *J. Phys.: Condensed Mater.* **3,** 3215 (1991).
26. D. B. Wiles and R. A. Young, *J. Appl. Crystallogr.* **14,** 149 (1981).
27. D. B. Wiles and R. A. Young, *J. Appl. Crystallogr.* **15,** 430, (1982).
28. C. Caglioti, A. Paoletti, and E. P. Ricci, *Nucl. Instrum. Methods* **3,** 223 (1958).
29. R. D. Shannon and C. T. Prewitt, *Acta Crystallogr. B* **26,** 1046 (1970).
30. R. D. Shannon, *Acta Crystallogr. A* **32,** 751 (1976).
31. P. D. Battle, C. R. A. Catlow, J. Drennan, and A. D. Murray, *J. Phys. C: Solid State Phys.* **16,** L561 (1983).
32. M. J. Verkerk, G. M. H. Van De Velde, and A. J. Burgraaf, *J. Phys. Chem. Solids* **43,** 1129 (1982).
33. N. Jiang, R. M. Buchanan, D. A. Stevenson, W. D. Nix, J.-Z. Li, and J.-L. Yang, *Mater. Lett.* **22,** 215 (1995).
34. M. Drache, J. P. Wignacourt, and P. Conflant, *J. Solid State Chem.* **149,** 341–348 (2000).
35. S. Giraud, M. Drache, P. Conflant, J. P. Wignacourt, and H. Steinfink, *J. Solid State Chem.* **154,** 435–453 (2000).